Combining Magnetic Hyperthermia and Photodynamic Therapy for Tumor Ablation with Photoresponsive Magnetic Liposomes

Riccardo Di Corato,[†] Gaëlle Béalle,[‡] Jelena Kolosnjaj-Tabi,[†,§] Ana Espinosa,[†] Olivier Clément,[§] Amanda K. A. Silva,[†] Christine Ménager,[*,‡] and Claire Wilhelm[*,†]

[†]Laboratoire Matière et Systèmes Complexes, UMR 7057, CNRS and University Paris Diderot, 75205 Paris cedex 13, France, [‡]Laboratoire PHENIX, Sorbonne Universités, UPMC, University Paris 06, UMR CNRS 8234, 4 place Jussieu 75005 Paris, France, and [§]Inserm U970, Paris Cardiovascular Research Center-PARCC/Université Paris-Descartes, 75006 Paris, France

ABSTRACT The ongoing nanotech revolution has the potential to transform diagnostic and therapeutic methods. Stimuli-triggered nanotherapies based on remotely activated agents have become attractive alternatives to conventional chemotherapy. Herein, we designed an optimized smart nanoplatform based on dually loaded hybrid liposomes to achieve enhanced tumor therapy. The aqueous core was highly loaded with iron oxide nanoparticles, while the lipid bilayer was supplied with a photosensitizer payload. The double cargo translated into double functionality: generation of singlet oxygen under laser excitation and heat production under alternating magnetic field stimulation, coupling photodynamic therapy (PDT) to magnetic hyperthermia (MHT). These liposomes address both therapeutic agents within tumor cells, and the combined PDT/MHT therapy resulted in complete cancer cell death *in vitro* while total solid-tumor ablation was achieved in an *in vivo* rodent model.

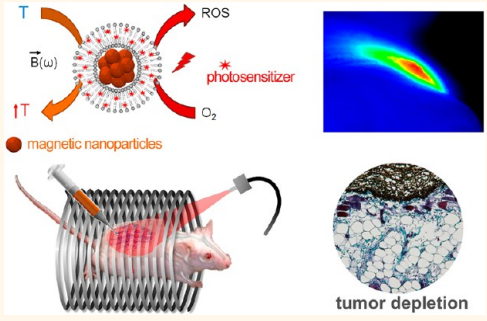

KEYWORDS: magnetic nanoparticles · photosensitizer · liposomes · magnetic hyperthermia · photodynamic therapy · cancer combined therapy

Current treatments for cancer face long-standing challenging obstacles. Classical therapeutic regimes can be ineffective or limited by dose-related toxicity and the damage they cause to healthy bystander tissues.[1−3] One promising strategy to limit adverse effects of cancer therapy is the use of nanocarrier systems that convey active drugs to target cells. The standard "bottom-up" approach consists of using self-assembled structures (liposomes, micelles, dendrimers) to obtain a synthetic nanovector capable of encapsulating, protecting, transporting, and delivering a therapeutic agent.[4] Liposomes are particularly promising for this purpose, being both nontoxic and biodegradable,[5] and their surface coatings with long polymer chains, such as polyethylene glycol (PEG), make them stealthier.[6,7] They can be injected intravenously, and their hollow, vesicular structure is inherently suited to transport a large amount of therapeutic agents, being hidden and protected, thus avoiding their degradation and fast elimination by the immune system. Liposomes can carry both hydrophilic molecules in their aqueous compartment and hydrophobic substances in their lipid bilayer.[8] Due to their functional versatility, liposomes thus remain the most intensively investigated delivery vehicles.[9] Besides, liposomes encapsulating anticancer active substances such as doxorubicin and daunorubicin are already approved by the FDA for use in clinical practice.[10]

In addition to current approaches aiming to improve the efficacy and tolerability of drugs, alternative strategies, based on triggerable materials that could be activated by external stimuli (*e.g.*, light, magnetic field), are being developed: because they are only toxic once activated, and their activation can be restrained to tumor tissue,[11] they are expected to improve treatment efficacy

* Address correspondence to claire.wilhelm@univ-paris-diderot.fr, christine.menager@upmc.fr.

Received for review December 5, 2014 and accepted February 19, 2015.

Published online February 19, 2015
10.1021/nn506949t

while minimizing damage to healthy tissues. The agents developed for this purpose include photosensitizers (for photodynamic therapy, PDT, already in clinical use),[12−15] metallic nanoparticles (*e.g.*, gold or silver for photothermal therapy, PTT),[16−20] and magnetic nanoparticles (*e.g.*, iron oxide for magnetic hyperthermia, MHT).[21−25]

Two recently marketed liposomal formulations designed for photodynamic therapy (Foslip and its PEGylated version Fospeg) have already shown their antitumoral potential.[21,26] The development of strategies that would allow magnetic nanoparticles encapsulation within liposomes is in its early stage and has so far been applied mainly to magnetic resonance imaging (MRI) tracking[27,28] and magnetic targeting.[29,30] The capacity of magnetic liposomes to induce local therapeutic hyperthermia has been rarely demonstrated.[31,32]

Here we propose a new liposome formulation combining both magnetic nanoparticles and a photosensitizer within the same nanoplatform, with a view to allow a dual photodynamic and magnetothermal therapy. By a one-pot synthesis method, we encapsulated a high concentration of magnetic nanoparticles within the liposome core and introduced a photosensitizer (m-THPC, already in clinical use under the name of Foscan[33]) into the lipid bilayer, yielding liposomes with highly satisfactory ratios of the two components. These multifunctional liposomes were first tested *in vitro*. We showed an optimal delivery of both agents to tumor cells and a therapeutic efficiency for each treatment, single or combined, with an impressive induced cell death for the combined approach. These strategies were then tested *in vivo* in a mouse model. Tumor growth was monitored after each treatment, photodynamic therapy and magnetic hyperthermia, independently or in combination. Each single treatment slightly inhibited tumor growth, while their combination led to a complete tumor regression, reflecting the synergistic potential of a combined therapy.

RESULTS AND DISCUSSION

Preparation of the Ultramagnetic Photosensitive Liposomes (UMPL). Figure 1a illustrates the rationale of the approach: liposomes that could be stimulated both by an alternating magnetic field, to induce local hyperthermia, and by a light source, to generate highly toxic reactive oxygen species (ROS). We recently adapted a reverse-phase evaporation method to obtain ultramagnetic liposomes (UML) with a high content of iron per lipids content,[30] essential for obtaining the local concentration needed to induce a pronounced temperature increase by magnetic hyperthermia. The hydrophobic photosensitizer, m-THPC, was selected to be enclosed in the lipid bilayer. This drug, first marketed in 2001 (Foscan), is already used in cancer therapy and is reported to be one of the most effective photosensitive agents.[33] Besides, its near-IR excitation profile ensures tissue penetration.[34] The m-THPC insertion within UML bilayers was first adjusted by differential scanning calorimetry (DSC) to ensure an optimal m-THPC/lipid ratio. For pure dipalmitoylphosphatidylcholine (DPPC) liposomes, we measured a transition temperature of 40.8 °C (Figure S1, Supporting Information). A decrease in peak cooperativity was observed with increasing m-THPC concentration (3.2, 6.2, and 9 mol %), demonstrating the photosensitizer insertion in the bilayer. For more than 11.5 mol % of m-THPC, a second peak appears around 36 °C, showing a phase separation in the bilayer. For pure distearoylphosphatidylcholine (DSPC, Figure S2), the insertion of the photosensitizer did not perturb the lipid arrangement until a concentration of 14.1 mol % of m-THPC. This result is not surprising, considering that DSPC is more hydrophobic than DPPC because of its longer chains. For the applied lipid composition (DPPC/DSPC/DSPE-PEG2000 85.5/9.5/5 mol) and at 6.2 mol % of m-THPC, the lipid bilayer structure was modified, as demonstrated by the shoulder appearing on the curve (Figure 1b). This shoulder indicated the beginning of segregation in the lipid arrangement. At 14.1 mol % of m-THPC, the bilayer was strongly modified as the transition temperature almost disappeared. For this reason, 14.1 mol % of m-THPC was the maximum amount used for the experiments. At the end of the synthesis, a magnetic sorting was systematically used to collect all magnetic liposomes. This step allows the separation between the magnetic liposomes and free magnetic nanoparticles that are not attracted by the magnet. The iron/m-THPC concentration ratio after the sorting step was found to be [m-THPC](μM)/[Fe](M) = 120 $\pm$ 15 (average over eight preparations).

Observations by TEM (Figure 1c) of the UMPL thus obtained demonstrate a spherical structure, with average diameter of about 150 nm (Figures S3 and S4) and dense magnetic content. Each liposome was fluorescent (observed as single fluorescent spots), with an emission spectrum typical of the m-THPC molecule (Figure 1d). The good colloidal stability reflected by the individual fluorescent spots was confirmed by the dynamic light scattering (DLS) distribution (Figure 1e), with a thin peak centered at 200 nm in diameter. Besides, the fluorescence emitted by m-THPC matched the liposomes magnetic content, as demonstrated by magnetophoresis (Figure 1f and Figure S5): when experiencing a magnetic field gradient, all fluorescent dots moved toward the magnet. The derived magnetic velocity directly provides the exact number of magnetic nanoparticles per liposome by balancing the viscous force (provided by the velocity) and the magnetic force (proportional to the magnetization, that is, the number of nanoparticles), as detailed in the Experimental Section. On average, one liposome contains 6 fg of iron, corresponding to a volume fraction of 20% (equivalent to 2400 nanoparticles per

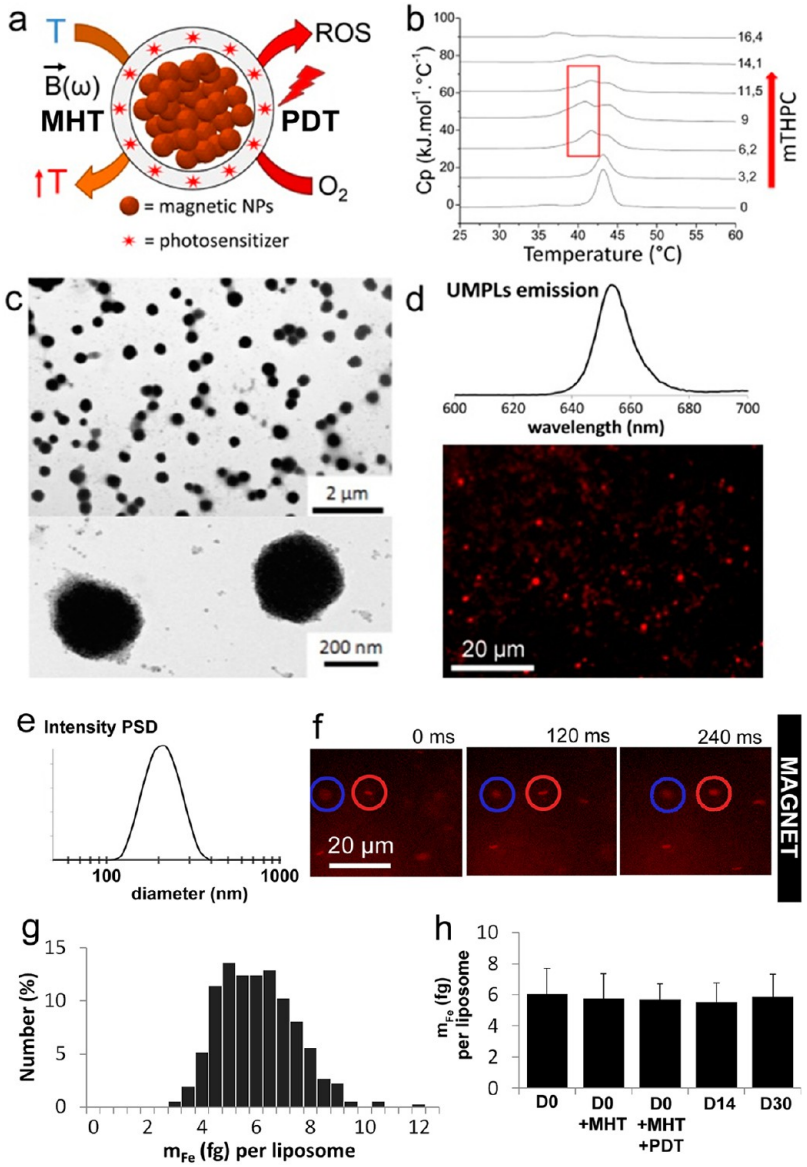

Figure 1. Ultramagnetic photosensitive liposomes. (a) Schematic description of UMPL structure and activation principle. The two payloads have a different localization: magnetic nanoparticles are confined in the core, whereas the photosensitizing drug is intercalated in the lipid layer. The applications of alternating magnetic field or laser radiation actuate the therapeutic effect, respectively, by increasing temperature and production of ROS. (b) DSC curves of liposomes (DPPC/DSPC/DSPE-PEG) obtained with increasing amount of drug: the higher affinity of the drug to DSPC portion caused a partial segregation of lipid mixture, highlighted with a red mark. (c) TEM characterization of UMPL. (d) Fluorescence emission profile (λ_{ex} = 430 nm) and confocal microscope analysis (λ_{ex} = 405 nm) of UMPL. (e) DLS analysis of UMPL reporting a thin size distribution centered at 200 nm. (f) Magnetophoresis setup (magnetic field gradient of 190 T/m) was used to track the magnetic attraction of liposomes in the fluorescent channel (m-THPC). It shows the colocalization of magnetic nanoparticles (because it moves toward the magnet) and photosensitizers (because of the fluorescence). (g) Distribution of the amount of iron (magnetic content) per liposome, retrieved from the magnetophoresis experiments (400 independent measurements). (h) Evolution of the magnetic content per liposome, over time or after stimulation (magnetic hyperthermia, with or without photodynamic excitation): the iron mass per liposome is perfectly constant.

liposome). The distribution of the magnetic content per liposome (Figure 1g) is an additional conclusive proof of the stability (standard deviation of 24% among the liposome population, unambiguously demonstrating that all liposomes are single entities).

UMPL Stability and m-THPC Release over Time and after Stimulation. Liposome stability was first investigated in storage conditions (4 °C). Within 30 days, no differences were detected in their morphology nor colloidal stability, analyzed by TEM and DLS (Figure S4), and the iron content per liposome remained constant at 6 fg of iron (Figure 1h and Figure S5). The m-THPC release from the liposomes was investigated, as well, by comparing the m-THPC concentration in the supernatant after liposome centrifugation (13 000 rpm for 30 min) to the concentration before centrifugation. At day 0, 0.05% release was measured, and this extremely low release increased to only 1% at day 30.

Second, the impact of magnetic and laser stimulations on liposome integrity and stability was explored. The iron content per liposome remained constant after magnetic or laser stimulations (Figure 1h and Figure S5), demonstrating that the liposomal structure was not degraded (which would have resulted in the release of free nanoparticles). This was confirmed by TEM (Figure S6): magnetic hyperthermia, alone or in combination with laser irradiation, did not impact the liposome morphology. The m-THPC release was measured after liposome centrifugation (same as above), and the release detected after magnetic or laser stimulation was unchanged compared to the control.

Finally, the stability of the liposomes was also evaluated by a dialysis experiment. After a small burst release (about 20%) of drug that occurs in the first 6 h, no massive additional release was observed during 7 days of analysis (Figure S7).

Uptake by Tumor Cells *in Vitro*. Liposomes were first incubated *in vitro* with ovarian cancer cells for short periods (1−4 h) and several concentrations, ranging from 5×10^9 to 5×10^{10} liposomes per mL ([Fe] = 0.5−5 mM). The cellular uptake of iron (measured by magnetophoresis,[35] Figure 2) was already maximal after 1 h incubation in the presence of about 1 mM extracellular iron, reaching an iron content of 15−20 pg per cell.

Cellular localization of the liposomes was then investigated by confocal microscopy (Figure 3), after an incubation at [Fe] = 5 mM ([m-THPC] = 0.6 μM), equivalent to 5×10^{10} liposomes per mL. Lipids from liposomes were labeled with rhodamine B (green excitation, red emission, colored in red in Figure 3), while m-THPC could be tracked by its intrinsic fluorescence (UV excitation, dark red emission, colored in magenta in Figure 3). Besides, cells were postincubated with LysoTracker Green DND-26 (blue excitation, green emission, colored in green in Figure 3) in order to label endosomal compartments and clearly identify the intracellular planes in *Z* stacks. First, cells were observed immediately after a liposome incubation of 10 min (Figure 3a and Figure S8) to image the early stage of liposome interaction with cells. Spot-like structures of both rhodamine and positive m-THPC could be observed surrounding the cells. Such a dual fluorescent spot pattern demonstrates that liposomes reach the cells as structurally intact entities carrying the photosensitizer content. When images were captured at higher *Z* planes over the cell (where the LysoTracker staining is very low), fluorescent spots were clearly localized at the outer cell membrane at the top of the cells. Conversely, fluorescent spots were observed surrounding the cells at the membrane for images in intracellular planes (positive to LysoTracker). On *Z*-view reconstruction, rhodamine and m-THPC spots are invariably detected above the LysoTracker spots for such early time point observations.

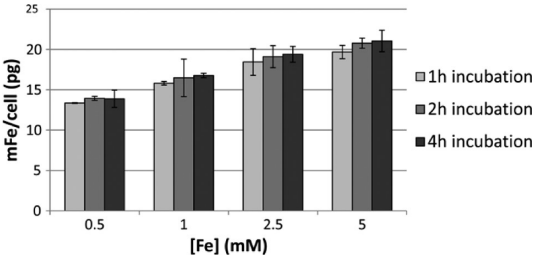

Figure 2. Quantification of UMPL cell internalization. Evaluation of liposome uptake in terms of mass of iron per cell (single-cell magnetophoresis analysis). Liposomes were incubated for 1, 2, or 4 h at different concentrations (from 0.5 to 5 mM of iron). Saturation of cell loading was reached at 2.5 mM extracellular iron.

Cells were then observed after 1 h incubation with the liposomes (followed by overnight postincubation), and analysis was equally performed to image liposome and m-THPC final localization (Figure 3b and Figure S9a). Rhodamine sustained a spot-like staining pattern, thus directed to intracellular compartments, as invariably detected in the same planes of the LysoTracker, with partial colocalization. m-THPC equally localized intracellularly, as also confirmed by detection in the same plane of the LysoTracker. Interestingly, m-THPC localization unambiguously shifted to a diffuse cytoplasmic distribution pattern, quite distinct from the initial spot-like staining observed at the early observation time point. Liposomes were thus totally internalized, although lipids and photosensitizers diverged to target different intracellular structures. In order to localize, as well, the magnetic nanoparticles, a fixation step was performed in the presence of a horizontal magnetic field (parallel to the plane of the cells). Chaining (Figure 3c and Figure S9b), indicative of magnetic alignment, was observed both in the bright field and in the rhodamine channel, while m-THPC remained diffuse within the cytoplasm, in the same pattern observed in the absence of magnetic field (Figure 3b). Such alignment induced by a magnetic field shows that the magnetic nanoparticles are confined within membrane-delimited compartments, together with the lipids, and not diffused within the cytoplasm. This was confirmed by TEM observations, clearly identifying magnetic nanoparticles in endosomal-like structures (Figure S10).[30] Liposomes thus attain tumor cells as an intact entity, carrying both the magnetic nanoparticles and the m-THPC photosensitizer. Lipids, nanoparticles, and photosensitizer then target different intracellular localizations. The hydrophobic photosensitizer is scattered throughout the cytoplasm, probably due to its ability to cross membranes, while lipids and nanoparticles, first entering by endocytosis, are sequestered inside endosomal-like intracellular compartments. Remarkably, the same diffuse m-THPC pattern was obtained when free

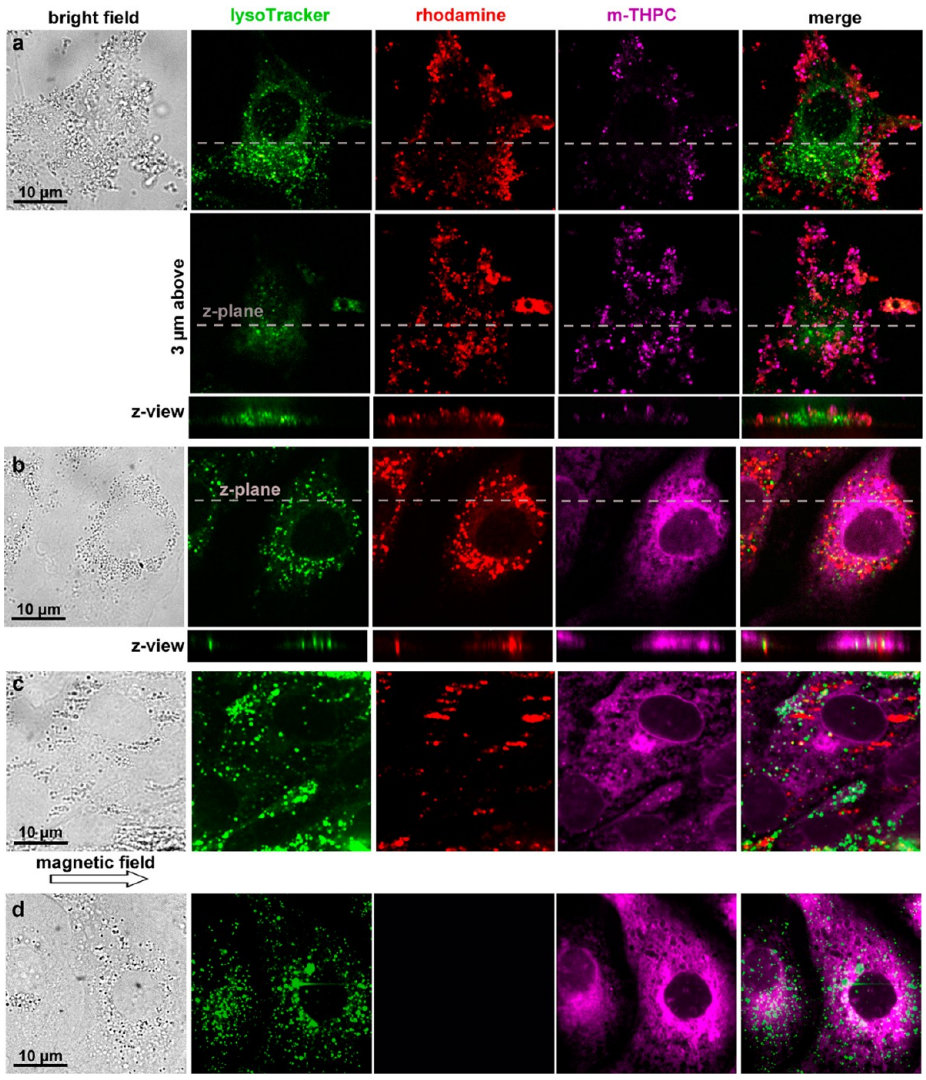

Figure 3. Confocal microscope analysis of the cellular localization of liposomes, m-THPC, and magnetic nanoparticles. For each condition, bright-field and three fluorescence images (excitation at 488 nm and emission at 525 nm for the LysoTracker, colored in green; excitation at 561 nm and emission at 604 nm for the rhodamine lipid, colored in red; excitation at 405 nm and emission at 685 nm for m-THPC, colored in magenta) were acquired. (a) Early stage of liposome interaction with cells (10 min incubation at [Fe] = 5 mM). In the cells' basal plane (positive to LysoTracker), the liposomes localize at the plasma membrane, surrounding the cell, and rhodamine lipids colocalize with m-THPC. At 3 μm above, they are seen on the top of the cells, again at the membrane. This membrane localization is also demonstrated on the *Z* view (reconstruction from *Z* stacks, acquired with a 0.5 μm interslice), corresponding to the plane indicated by gray dots. (b) Late stage of liposome interaction with cells (1 h incubation followed by overnight chasing). Images of the basal plane and *Z*-view reconstruction (*Z* plane of the dotted gray line) demonstrate that rhodamine lipids as well as m-THPC are internalized, lipids ending within endosomal compartments, while m-THPC is diffuse in the cytoplasm. (c) Late stage of liposome interaction with cells and magnetic chaining (1 h incubation followed by overnight chasing under the application of a 0.2 T horizontal magnetic field). Lipids, magnetic nanoparticles, and m-THPC are all intracellular. m-THPC is still dispersed within the cytoplasm; magnetic nanoparticles are confined inside compartments, which align in the direction of the magnetic field (as observed in the bright-field image). The chaining is also detected on the rhodamine fluorescence channel, demonstrating colocalization of the lipids constituting the liposomes and the magnetic nanoparticles. (d) Localization of free m-THPC (incubated 1 h at [m-THPC] = 0.6 μM followed by overnight chasing). m-THPC is found distributed all through the cytoplasm, as observed when it was delivered by the liposomes.

m-THPC was incubated with cells for 1 h, at the same concentration of [m-THPC] = 0.6 μM (Figure 3d, Figure S9c, and Figure S11, where an additional nucleus (DAPI) staining is shown).[36] This cytoplasmic redistribution of m-THPC is very promising for therapeutic applications, as it allows ROS to be generated closer to their cellular targets (*e.g.*, mitochondria) and thereby to induce cell death.

Combined Magneto-phototherapy *in Vitro*. The liposomes' therapeutic efficacy was first tested *in vitro* (Figure 4) on 3D pellets consisting of compact aggregates of a few million tumor cells (20 million cells in 150 μL). These pellets were exposed to magnetic hyperthermia and photodynamic therapy, alone and in combination, always starting with the hyperthermia protocol. Figure 4a shows the effectiveness of each

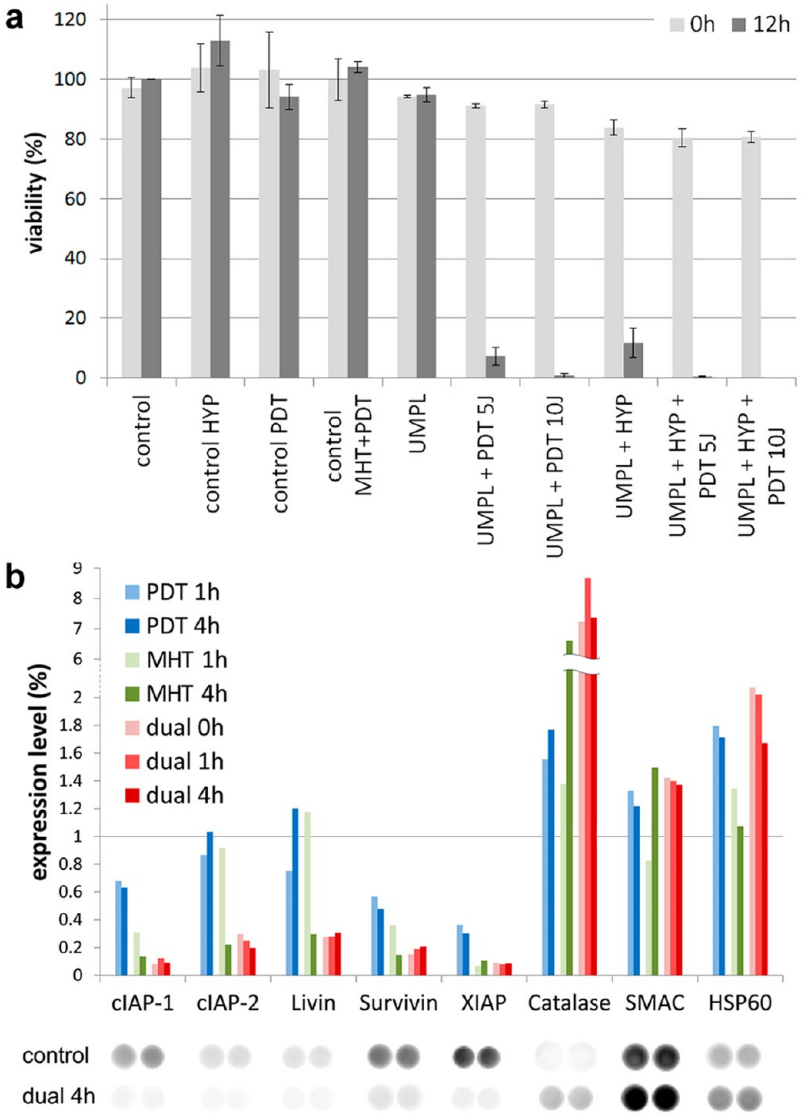

Figure 4. Therapeutic efficiency *in vitro*. (a) Cancer cells loaded with UMPL were subjected to different protocols: no treatment for control and liposome-doped cells; PDT, with fluencies of 5 or 10 J/cm^2, alone or in combination with magnetic hyperthermia, for unlabeled control cells and liposome-doped cells. Cell viability was assayed just after treatments by Trypan Blue exclusion assay and after 12 h by Alamar Blue (performed on reseeded treated cells). (b) Expression of some apoptosis-related proteins was monitored in cellular preparations after treatments. Cell lysates were processed by Proteome Profiler Array (R&D Systems, Inc.). All tested IAP proteins (inhibitors of apoptosis proteins: cIAP-1, c-IAP-2, Livin, Survivin, XIAP) were down-regulated after treatments, whereas some stress-related proteins (catalase, SMAC, HSP60) were overexpressed.

treatment in terms of cell viability, immediately after treatment (0 h) and 12 h later. Importantly, the vector itself was not toxic, as cells' viability remained unaffected by simple liposome internalization, without any stimulation. Similarly, neither the magnetic hyperthermia nor the photodynamic treatments, nor both, had any impact on control cells' viability. The viability measured immediately after treatment was slightly affected by applied therapies. In contrast, 12 h after treatment, cell viability was strongly reduced: only 10% of cells were still alive after magnetic hyperthermia alone, and only 5 and 1% were still alive after photodynamic therapy alone, with deposited light energies of 5 and 10 J, respectively. After dual treatment, tumor cell viability fell to 0.2% at 5 J and to 0% at 10 J with the same magnetic field conditions. Such total tumor cell destruction *in vitro* is necessary to ensure potential therapeutic effects *in vivo* and to avoid tumor growth that simply resumes a few days after treatment because of some surviving proliferating cancer cells. Finally, proteomic analysis of cell death (Figure 4b) confirmed these results and provided insights into the underlying mechanisms of the two treatments. A strong reduction of inhibitor of apoptosis IAP proteins (XIAP, Livin, Survivin, cIAP-1, and cIAP-2) was associated with an evident increase in levels of catalase, SMAC and HSP60. The latter three proteins are associated with an increase of ROS and mitochondrial damage, which are considered as cellular stress symptoms. Therefore, an activation of

intrinsic apoptosis pathways was shown for both therapeutic approaches.

Tumor Regression *in Vivo*. Dual therapy was then tested on tumor-bearing mice (Figure 5a). For magnetic hyperthermia alone, the tumor temperature was monitored in real time by an infrared camera, which indicated an increase of the temperature at the surface of the skin, adjacent to the tumor, for nearly 10 °C (Figure 5b, movie M1 in Supporting Information). In addition, the *in vivo* distribution of injected liposomes was monitored by high-resolution MRI, showing that the majority of injected liposomes remained at the site of injection (Figure S12). The evolution of tumor growth is presented in Figure 5c for all conditions. First, the intratumoral injections of UMPL did not affect tumor growth if neither the magnetic field nor the laser were applied, confirming the nontoxicity of the dual platform, in comparison to the control. Second, neither the PDT nor the magnetic hyperthermia treatments impacted the growth of noninjected tumors. As a stand-alone procedure, magnetic hyperthermia with ultramagnetic liposomes was sufficient enough to decrease tumor growth consistently. Photodynamic therapy alone also reduced tumor growth but to a smaller extent. However, the combination of both therapies remarkably led to complete tumor regression. For this condition, immediately after treatment, the tumors slightly swelled and the tumoral mass became softer. On day 3, the tumor volume started to decrease and a scab started to form on the surface of the skin adjacent to the tumor (Figure S13). On day 5 after treatment, the tumoral zone completely flattened and only a scab was visible on the skin.

Histological sections (Figure 6) of the tumors revealed peripheral liposome accumulation in the tumor capsula when PDT or MHT treatment was not applied. Conversely, as soon as both treatments were applied separately, liposomes penetrated diffusively into the tumor. In the vicinity of liposome-rich zones, large necrotic areas were observed when either PDT or MHT was applied. In the group treated with the dual therapy, where complete tumor regression was observed macroscopically, the liposomes were spread across the scar tissue.

Photosensitive Magnetic Liposomes: A Combined Therapy. The complete tumor regression achieved with the dual therapy *in vivo* is particularly promising. Interestingly, photodynamic therapy was more effective than magnetic hyperthermia *in vitro*, while the opposite was observed *in vivo*. Still, the combination of the two therapies brought the best results both *in vitro* and *in vivo*. Indeed, PDT may be weakened by a suboptimal concentration of the therapeutic agent within the tumor, photobleaching of the photosensitizer upon light irradiation, and low production of singlet oxygen due to local hypoxia.[33,37,38] New synergistic approaches combining PDT with other therapeutic modalities, involving hyperthermia, may hold the promise to overcome current limitations of PDT. The advantages of such a combination may concern the intrinsic mechanisms related to each modality. In this context, it has been reported that moderate temperature increase may enhance blood flow and tumor oxygenation, reducing undesired hypoxia for PDT.[39,40] Additionally, the mechanism of the synergistic interaction may take place at the cellular level since PDT weakens the heat shock cell defense mechanism.[41] In the survey of such synergistic effects, recent research efforts have been focused on combining PDT and PTT.[42−45] These approaches involving the combination of PDT and PTT mainly rely on plasmonic nanoparticles. For instance, chlorin e6 linked to the surface of gold nanorods was used to target cancer cells for PDT/PTT, with a cell viability of about 80% of cells for the PDT group, 63% for PTT group, and decreasing to 40% in PDT/PTT group.[44] This result shows the synergism of dual treatment, but it is less striking than the *in vitro* ones reported herein. In an *in vivo* approach, gold vesicles loaded with chlorin e6 were tested for PDT/PTT in mice bearing tumors. The results pointed out a synergistic effect of PDT/PTT superior to that of any single modality treatment applied solely.[42] In a related approach, a complex between gold nanorods and aluminum phthalocyanine tetrasulfonate was investigated to treat nude mice bearing SCC7 tumors. Enhanced *in vivo* therapeutic effect with total tumor regression was observed for a double-treated group (PDT/PTT), while only partial regression or growth slowdown was achieved in single-treated groups.[43] All reported approaches concerned gold nanoplatforms for PTT, while little attention was given to magnetic hyperthermia combined to PDT. A few studies proposed that a PDT could be associated with magnetic hyperthermia. However, they did not merge a photosensitizer and magnetic nanoparticles into a single nanoplatform nor provide proof of a synergic effect *in vivo*. For instance, Oliveira and colleagues investigated the spectroscopic properties of a mixture of phthalocyanine/magnetic fluid.[46] Although they indicated the potential interest of the mixture for magnetic hyperthermia combined to PDT, *in vitro* and *in vivo* tests were not performed. In a related study, another group designed porphyrin−magnetite nanocomposites with noncovalent ionic and hydrogen bonding interactions between the particle surface and porphyrin molecules. Although a single entity displaying both magnetic and photoresponsiveness was designed, there was no investigation of magnetic hyperthermia combined to PDT *in vitro* or *in vivo*.[47] Oil-in-water nanoemulsions and liposomes incorporating both a photosensitizer and magnetic nanoparticles have already been produced. However, they have been tested only *in vitro*.[48,49] To the best of our knowledge, the present study is the first to address the synergic

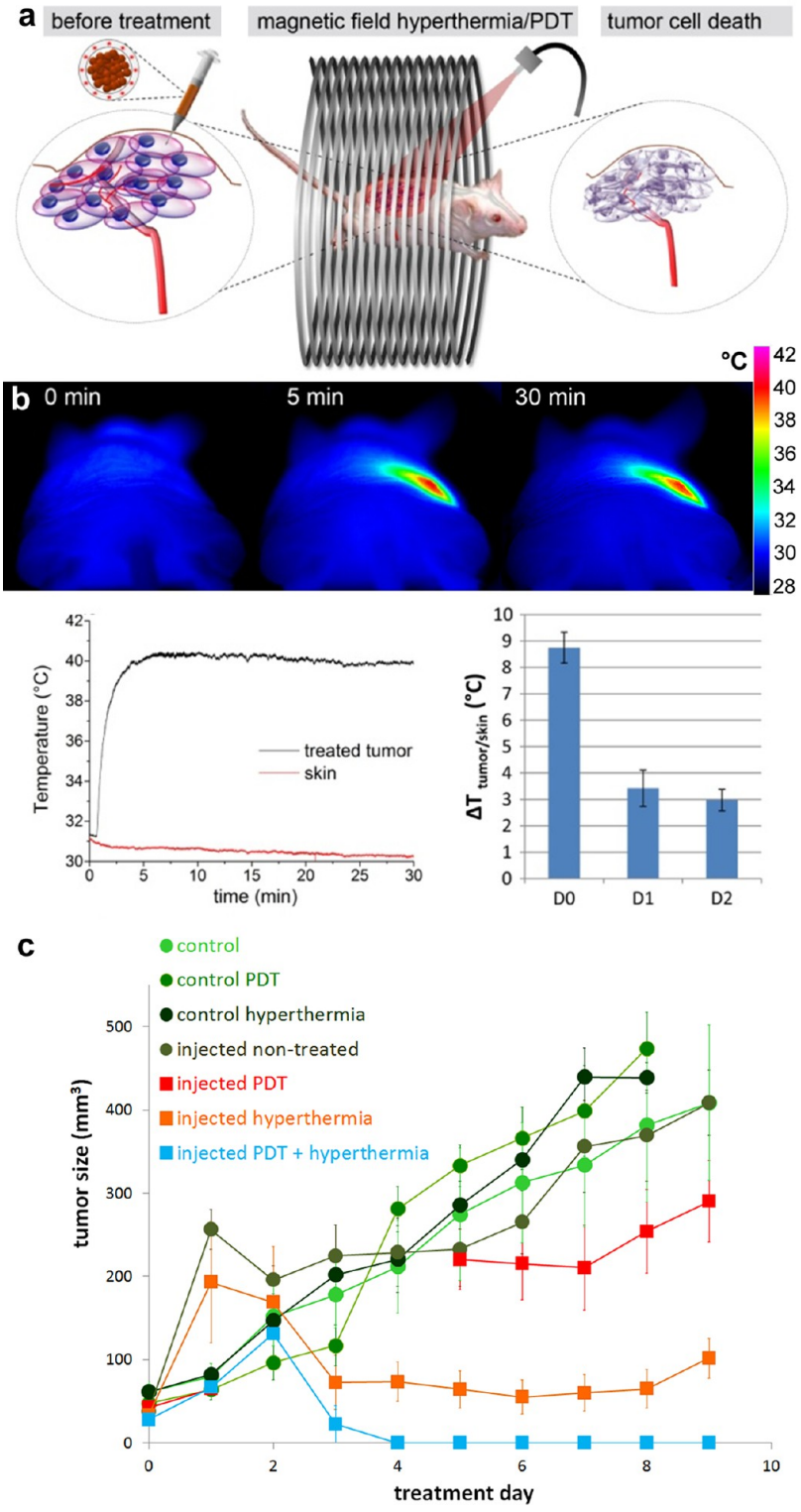

Figure 5. Treatment efficacy on tumor-bearing mice. (a) Therapeutic strategy sketch: liposomes were injected intratumorally, and mice were subsequently subjected to combined treatment with magnetic hyperthermia and laser irradiation. (b) Increase in local temperature during magnetic hyperthermia treatment was monitored with an infrared thermocamera. The maximum temperature was reached about 5 min after field application and maintained for the entire treatment cycle (30 min). A movie of the temperature recording is provided in the Supporting Information. Because of cell rearrangement, nanoparticle dilution, and aggregation, the heating efficacy decayed after one cycle of treatment, assessing a local temperature increase of a few degrees during magnetic hyperthermia. It is noteworthy to highlight that the camera measures the surface temperature of the skin, so the temperature within the tumor is expected to be higher. (c) Tumor growth curves of different control groups and treatment groups. D0 on the graph corresponds to the day of liposome injection, which also corresponds to the first day of treatment. Descriptive statistical analysis for tumor growth curves is reported in Table S1. In Supporting Information Figure S14, a Kaplan–Meier plot of complete tumor remission is shown.

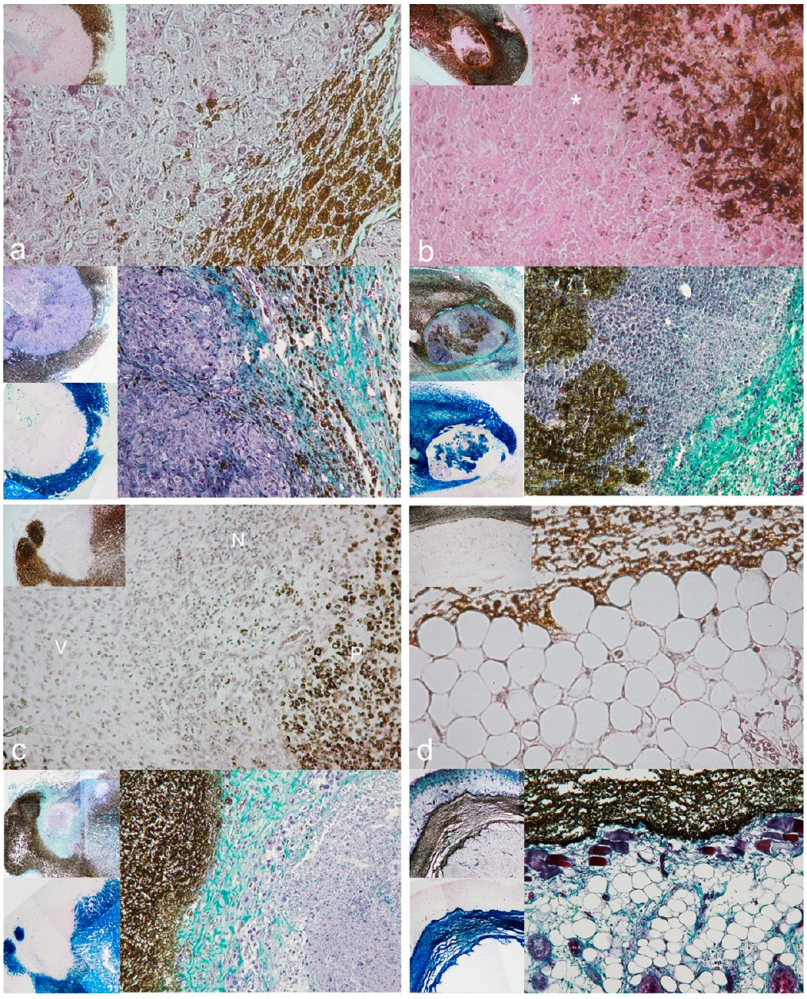

Figure 6. Histological analysis of excised tumors. In each section, hematoxylin/eosin (HE) staining (top panel), Masson's trichrome staining (middle left and bottom right panels), and Nuclear Red/Perls Prussian Blue staining (bottom left) are reported. (a) Optical micrographs of control tumors (injected but not exposed to the laser nor to the magnetic field) generally exhibited a viable core and the majority of the nanoparticles (brown in HE-stained sections and blue after Perls staining) were restrained at the tumor periphery, which is rich in collagen (green in Masson's trichrome stained sections). Tumor cells in proximity of nanoparticles remained viable when treatment was not applied. (b) Laser irradiation alone slowed tumor growth and affected the intratumoral distribution of liposomes, as they penetrated from the tumor capsula, rich in collagen fibers (green after Masson's staining) into the tumor core. In addition, necrotic zones characterized by lost cell cohesion and immune cell infiltration were prominent throughout the tissue. The asterisk on the magnified view (HE staining) denotes a large zone of hemorrhagic necrosis adjacent to the particles. (c) Magnetic hyperthermia alone produced large areas of necrosis (N) in proximity of particles (P), although some viable tissue (V) was detected distal to particles. In comparison with other groups, thicker areas of fibrous tissue were detected after Masson's trichrome staining. (d) In sections of the tumors treated with the dual therapy, little, if any, tumor cells were detected. Particles were mainly localized in the scar tissue, adjacent to adipose tissue. The remaining particles colocalized with the collagen fibers of the destructured tissue, while the treated tumoral mass was visibly depleted.

effect of PDT coupled to magnetic hyperthermia *in vitro* as well as *in vivo* by means a unique nanoplatform simultaneously integrating a dual magnetic and photosensitizer loading for ultimate hyperthermia/PDT combined therapy.

CONCLUSION

In conclusion, we have developed a novel type of liposome formulation combining magnetic nanoparticles and a photosensitizer. Detailed DSC characterizations were used to optimize the amount of photosensitizer present in the liposome bilayer. The antitumoral efficacy of the liposomal nanoplatform was first demonstrated *in vitro*: each treatment alone produced similar rates of tumor cell death, while combined treatments led to complete cell destruction, a prerequisite for *in vivo* treatment that is rarely achieved. Analysis of the cell death signatures revealed that the two treatments acted synergistically by triggering apoptotic signaling pathways. *In vivo*, each treatment alone was capable of inhibiting tumor growth, while combined treatment completely eradicated the tumor. This spectacular efficacy of combined magnetic therapy and phototherapy endorses the use of multiple approaches to cancer therapy. The next step will be to deliver these liposomes specifically to

tumor cells by magnetic or cellular targeting. If successful, this approach would avoid surgery and damage to healthy bystander tissues and would thus minimize clinical adverse effects.

EXPERIMENTAL SECTION

Ultramagnetic and Photosensitive Liposome Preparation. *Materials.* Chloroform solutions of 1,2-dipalmitoyl-*sn*-glycero-3-phosphocholine (DPPC), 1,2-distearoyl-*sn*-glycero-3-phosphocholine (DSPC), 1,2-distearoyl-*sn*-glycero-3-phosphoethanolamine-*N*-[(carboxy(polyethylene glycol)2000] (ammonium salt) (DSPE-PEG2000), and L-α-phosphatidylethanolamine-*N*-(lissamine rhodamine B sulfonyl) (ammonium salt) (egg-transphosphatidylated, chicken) were purchased from Avanti Polar Lipids, Inc. Chloroform and diethyl ether were supplied by Carlo Erba reagents and VWR. m-Tetrahydroxyphenylchlorin (m-THPC) was purchased from Inochem.

Size-Sorted Iron Oxide Magnetic Nanoparticle Synthesis. Nanoparticles were synthesized by alkaline co-precipitation of $FeCl_2$ and $FeCl_3$ salts.[50] After precipitation, nanoparticles were sorted by size by adding HNO_3 (0.45 M) to the suspension followed by magnetic decantation. This operation was repeated with the deposit until suitable size was obtained. Sodium citrate at a molar ratio nFe/nCit = 0.13 was added to the sorted nanoparticles, and the mixture was heated at 80 °C for 30 min to promote absorption of citrate anions onto their surface. The mean diameter of the nanoparticles used for the preparation of the liposomes was d_0 = 9 nm with a polydispersity index of σ = 0.35.

UMPL Preparation. UMPLs were prepared by the reverse-phase evaporation method, established by Skoza *et al.*[51] and Béalle *et al.*[30] and modified as follows: a mixture of DPPC/DSPC/DSPE-PEG 2000 (85/10/5 mol %, 250 μL) was mixed with a solution of m-THPC (in chloroform, 3.3 mg/mL) and diluted up to 1 mL with chloroform and up to 4 mL with diethyl ether. Afterward, magnetic nanoparticles (1 mL) dispersed in 5 mM sodium citrate buffer (0.7 M in iron) were introduced before sonication at room temperature for 20 min to produce a water-in-oil emulsion. Preparation was immediately transferred to a round-bottom flask, and organic solvents were evaporated with a rotavapor R-210 (Buchi) at 30 °C until the gel phase disappeared. The formulation was modified for the preparation of rhodamine-labeled liposomes with the following ratios: DPPC/DSPC/DSPE-PEG2000/Rho-PE 84.5/9.5/5/1. Afterward, the water-dispersed liposomes were filtrated through a 0.4 μm filter. Non-encapsulated nanoparticles were removed by magnetic sorting using a NdFeB magnet (0.3 T). The sorting was repeated twice for 12 h, and the resulting liposomes were resuspended in 5 mM sodium citrate buffer.

Transmission Electron Microscopy. UMPLs were drop-casted on a carbon-coated copper grid (300 mesh) and dried. Liposomes were characterized by a JEOL 100 CX TEM at 60 keV.

Total Iron Concentration. Concentration of iron was measured by atomic absorption spectroscopy with a PerkinElmer AAnalyst 100 apparatus after degradation of the magnetic nanoparticles and the liposomes. For that, 20 μL of liposomes was solubilized in 100 mL of HCl (37%) for 5 min.

Titration of Lipids (Rouser Method). After acidic degradation, inorganic phosphate content was measured by colorimetric titration (λ = 797 nm) after addition of ammonium molybdate.[52]

DSC Analysis. The behavior of m-THPC from 0 to 16.4 mol % has been tested with every constituent of the bilayer (pure DPPC, pure DSPC) and for the final composition DPPC/DSPC/DSPE-PEG by differential scanning calorimetry (TA Instrument).

Photoluminescence Analysis. PL spectra of the water suspension of UMPLs were acquired by a Cary Eclipse fluorescence spectrophotometer (Varian Inc.), applying a λ_{exc} of 430 nm and collecting UMPL emission from 600 to 700 nm.

Dynamic Light Scattering Analysis. DLS curves of the size distribution were obtained using NanoSizer (Zeta-Sizer, Malvern Instrument). There is no ultrasonic pretreatment of liposomes before DLS measurements.

***In Vitro* Experiments.** *Cell Culture.* Human adenocarcinoma SKOV-3 cells (ATCC #HTB-77) were grown in adhesion in McCoy's 5A modified medium (Sigma-Aldrich #M9309) supplemented with penicillin (50 IU/mL), streptomycin (50 μg/mL), and 10% fetal bovine serum (FBS). A431 human epidermoid carcinoma cells (ATCC #CRL.1555) were cultured as adherent cells in RPMI-1640 medium supplemented with 10% FBS and Geneticin (800 μg/mL). Both lineages were maintained at 37 °C in humidified atmosphere at 5% CO_2.

Incubation Details and Treatment Application. For the *in vitro* tests, SKOV-3 cells were incubated with a suspension of UMPL (from 0.5 to 5 mM in iron, in serum-free RPMI-1640 medium supplemented with 5 mM sodium citrate) for 1, 2, or 4 h. After incubation, a chase period in complete medium (McCoy5A medium supplemented with 10% FBS) was applied for 2 h. Subsequently, the cells were detached by means of trypsin-EDTA solution and resuspended in PBS in order to obtain 300 μL with a cellular concentration of 10^8 cells per mL. This compact suspension was then transferred into a 0.5 mL tube suitable for treatment application. For the application of magnetic hyperthermia, a laboratory-made device was used. It consists of a resonant RLC circuit, using a 16 mm coil producing an alternating magnetic field with a frequency ranging from 300 kHz to 1.1 MHz and with amplitudes up to 27 kA/m. Temperature was probed with a fluoroptic fiber thermometer and recorded every 0.7 s. The UMPL-labeled cells were introduced in a test tube placed into the copper coil. The latter has a variable capacity in the range of 10 pF to 4 nF and a self-inductance of 25 μH. The coil was cooled with circulating nonane. Temperature of the nonane was controlled to obtain an equilibrium temperature of 37 ± 0.2 °C in the samples. Specific loss power (SLP) was calculated (eq 1) from the initial linear increase of temperature as a function of time (d*T*/d*t*):

$$\mathrm{SLP} = \frac{CV_s}{m}\frac{\mathrm{d}T}{\mathrm{d}t} \quad (1)$$

where C_{water} = 4185 J L^{-1} K^{-1} is the volume-specific heat capacity of the sample, V_s the sample volume, and *m* the mass of magnetic material in the sample. Labeled cells were treated for 30 min with a field with an amplitude of 24 kA/m and a frequency of 700 kHz.

For the application of PDT, the cell suspension was spread onto a 35 mm plate, with a liquid thickness of 1−2 mm. Then, a laser diode driver (KS3-11312-101, BTW Beijing Ltd.) with an output power of 400 mW at 650 ± 10 nm was applied for 4 or 8 min to obtain a fluency of 5 or 10 J/cm^2. The optical fiber was fixed at 6 cm from the cell suspension in order to apply an average laser spot of 9.6 cm^2.

Magnetophoresis. Magnetophoresis was used to quantify either the amount of iron either per single liposome or per single cell (having internalized the magnetic liposomes).

For the measurement of the liposome magnetic content, a miniaturized nickel tip was placed in a homogeneous magnetic field of 0.2 T, generating a local magnetic field gradient of gradB = 195 T/m in the observation window. Single liposomes were tracked during their motion toward the magnet in the fluorescent channel (excitation 470 nm/emission 650 nm) specific for m-THPC. From the velocity ($v_{liposome}$) computed, the magnetic moment, $M_{liposome}$ (expressed in A·m^2, at 0.2 T), of each single tracked liposome is calculated: $M_{liposome} = 3\pi\eta d_{liposome}v_{liposome}/\mathrm{gradB}$. It can then be converted into a mass of iron (1 pg_{Fe} corresponds to 8.4 × 10^{-14} A·m^2 at 0.2 T).

For the measure of the liposome uptake potency by tumoral cells, SKOV-3 cells were incubated with different amounts of liposomes (as described above). Subsequently, the cells were washed twice with PBS and detached by means of trypsin-EDTA. The collected fractions were then assayed for iron content by magnetophoresis. The magnetophoretic mobilities of individual magnetically labeled cells were measured in magnetic field and a field gradient of 145 mT to 17 T/m, created by a

permanent magnet (NdFeB, Calamit). From the balance between the viscous and magnetic forces experienced by the moving magnetic objects in the field gradient, a magnetic load is deduced and expressed as iron mass content per single cell.

Confocal Analysis. Confocal microscope images were acquired by using a Andor Technology with Olympus JX81/BX61 Device/Yokogawa CSU device spinning disk microscope (Andor Technology plc, Belfast, Northern Ireland), equipped with a 60xPlan-ApoN oil objective lens (60×/1.42 oil, Olympus). SKOV-3 cells were cultured on glass slides and incubated with liposome as described above. The cells were fixed at 4 °C for 30 min with 4% paraformaldehyde and counterstained with DAPI for 10 min at 4 °C. The fluorescence signals were detected with λ_{exc} = 405 nm and λ_{em} = 465 ± 30 nm for DAPI, λ_{exc} = 561 nm and λ_{em} = 604 ± 15 nm for rhodamine and λ_{exc} = 405 nm and λ_{em} = 660 ± 20 nm for m-THPC.

Cytotoxicity Assays. After the two treatments (alone or in combination), the viability of treated cells was evaluated by two different assays: Trypan Blue exclusion assay for acute toxicity and Alamar Blue for long-term toxicity. The Trypan Blue is a diazo dye that is not able to penetrate the plasma membrane of a live cell. When the integrity of the membrane is altered, in case of necrosis or apoptosis, the dye traverses the membrane and the cells become stained with blue. For the analysis, a small volume of cells were mixed with Trypan Blue 0.4% solution and immediately analyzed by optical microscopy by means of a Malassez hemocytometer. The percentage of viable cells is given by eq 2:

$$\text{viability}\,(\%) = (100\times N)/(N + N') \quad (2)$$

where N is the live cells (nonstained) and N' is the dead ones (blue stained).

The Alamar Blue assay (Life Technologies) is a quantitative test based on the ability of metabolically active cells to convert the reagent into a fluorescent and colorimetric indicator. After the dual treatments, the cells in suspension were counted and seeded, in equal amount, in 24-well plates in complete culture medium. After 12 h, the monolayer was washed twice with PBS and 300 μL of Alamar Blue solution was added to each well, following the protocol provided by manufacturer. After 2 h of incubation, 200 μL of each solution was transferred into a 96-well plate for analysis. The resulting fluorescence was analyzed by a microplate reader (BMG FluoStar Galaxy), with an excitation wavelength of 550 nm and by collecting the fluorescence at 590 nm. All the experimental points reported have been reproduced in triplicate.

Proteome Analysis. For the analysis of treatment effects on the cellular proteome, an antibody-based kit was used (Human Apoptosis Array, R&D System, #ARY009). For each experimental point, 10^7 cells (corresponding to 2 × 150 cm^2 culture flask) were processed following manufacturer's protocol with no changes. For the points at 1 and 4 h post-treatments, cells were diluted in PBS and kept at room temperature in a open vent tube in sterile conditions. Antibody spot intensities were analyzed by a LAS-4000 chemiluminescence imaging system (FujiFilm) and processed by open-source ImageJ software.

***In Vivo* Experiments.** *General Lines.* Animals were handled according to the European Community guidelines for the care and use of laboratory animals (European Directive 86/609/EEC on the protection of animals used for experimental and other scientific purposes and its amendment (2003/65/EC)). The Institutional Animal Care and Use Committee of Paris Cardiovascular Research Center (PARCC) approved animal protocols. Six-week-old female NMRI nude mice (weighing 32 g, provided by Janvier, France) were housed in polypropylene cages and were provided with food and water *ad libitum*. Each experimental group consisted of eight animals. The groups were defined as follows: (i) noninjected control group, (ii) injected control group with no treatments, (iii) magnetic hyperthermia, (iv) photodynamic therapy, (v) combined therapy. No effects were observed on tumor growth when laser/alternating magnetic field were applied to noninjected tumors (data not shown).

Treatment Protocols and Groups. Tumor model. Mice were anesthetized with isoflurane in air (supplied at a flow rate of 1 L/min), and 1.5 × 10^6 epidermoid carcinoma A431 cells suspended in 0.9% NaCl solution were inoculated subcutaneously on both flanks. After 1 week, the tumors attained a volume of 40−50 mm^3 and were ready for treatment. Tumor volumes were measured on a daily basis. The volumes were calculated by applying formula 3:

$$V_{tumor} = \frac{D \times d^2}{2} \quad (3)$$

where D is the longest tumor axis and d is the shortest one. Prior to treatment application, mice were anesthetized with intraperitoneal administration of ketamine/xylazine (10 and 50 mg/kg, respectively), and 50 μL of a UMPL suspension (1 M in iron, equivalent to 2.8 mg of Fe, and 150 μM for m-THPC) was intratumorally injected. About 5 min after injection, mice underwent magnetic hyperthermia and/or laser irradiation (PDT). This fast treatment was aimed to address the extracellular tumor matrix, to induce damage in the tumor area before treating tumor cells in subsequent cycles at 24 and 48 h from injection. For MHT, a commercial setup from Nanotherics Ltd. (magneTherm) was used. Mice were introduced in the coil enclosure, and a field of 30 mT at 111 kHz was applied for 30 min. The mapping of the mouse skin surface temperature was monitored using a FLIR SC7000 infrared camera. All the acquisitions were processed by Altair software (FLIR Systems, Inc.). For PDT, the laser was applied for 100 s by applying a spot of 1 cm^2 with an output power of 100 mW, in order to obtain a fluency of 10 J/cm^2. The treatments were repeated three times, with an interval of 24 h. Ten days after UMPL injection, the mice were sacrificed by cervical dislocation under ketamine/xylazine anesthesia. No mice were maintained alive after day 10 because the size of the collateral tumor (nontreated) exceeded ethical limits. Tumors (injected and collateral), spleens, and livers were excised and fixed in pH 7.4 phosphate-buffered 10% formalin and embedded in paraffin. Five micrometer tissue sections were stained by hematoxylin/eosin, Prussian Blue/Nuclear Red and Masson's trichrome stain. Table S2 details staining protocol characteristics.

Magnetic Resonance Imaging. Magnetic resonance imaging was performed on a Biospec 47/40 USR (40 cm bore actively shielded 4.7 T magnet) scanner interfaced to ParaVision software (both provided from Bruker Biospin GmbH, Rheinstetten, Germany). The whole-body imaging protocol was performed with a volume transmission/reception RF coil for mice (Bruker), using a gradient echo sequence (TR/TE = 300/3 ms, flip angle = 30°, FOV = 3 cm, 8 averages and a pixel resolution of 117 × 117 μm) with slices (thickness = 1 mm) positioned over the liver, spleen, and tumors. Two mice per group underwent MRI at day 6 after liposome injection. During the protocol, the animals were anesthetized with 2% isofluorane (Aerrane, Baxter, Maurepas, France) supplied in air mixture, while their body temperature was kept constant by circulating thermostated warm water. Image processing and analysis were made with the open source software OsiriX (3.9.2. version).

Conflict of Interest: The authors declare no competing financial interest.

Supporting Information Available: Additional figures, tables, and movie. This material is available free of charge *via* the Internet at http://pubs.acs.org.

Acknowledgment. This work was supported by the European project Magnifyco (Contract NMP4-SL-2009-228622). A.E. acknowledges support from the European Commission under a Marie Curie Intra-European Project FP7-PEOPLE-2013-IEF-62647. Additionally, we thank the European COST action TD1402 RADIOMAG. We are grateful to D. Talbot for the preparation of the magnetic nanoparticles, S. Neveu for TEM preparation, A. Michel for flame spectroscopy, J. Servais for hyperthermia setup, S. Canevari for providing the tumor cells, N. Luciani for help in proteome analysis, the anatomopathology platform of the Georges Pompidou Hospital (Paris) for Masson trichrome staining, L. Pidial and the personnel of the Paris Cardiovascular Research Center (PARCC) animal facility for their help in animal studies, and F. Gazeau for discussion.

REFERENCES AND NOTES

1. Pavet, V.; Portal, M.; Moulin, J.; Herbrecht, R.; Gronemeyer, H. Towards Novel Paradigms for Cancer Therapy. *Oncogene* **2011**, *30*, 1–20.
2. Lee, P. Y.; Wong, K. K. Nanomedicine: A New Frontier in Cancer Therapeutics. *Curr. Drug Delivery* **2011**, *8*, 245–253.
3. Albini, A.; Pennesi, G.; Donatelli, F.; Cammarota, R.; De Flora, S.; Noonan, D. M. Cardiotoxicity of Anticancer Drugs: The Need for Cardio-oncology and Cardio-oncological Prevention. *J. Natl. Cancer Inst.* **2010**, *102*, 14–25.
4. Bertrand, N.; Wu, J.; Xu, X.; Kamaly, N.; Farokhzad, O. C. Cancer Nanotechnology: The Impact of Passive and Active Targeting in the Era of Modern Cancer Biology. *Adv. Drug Delivery Rev.* **2014**, *66*, 2–25.
5. Maherani, B.; Arab-Tehrany, E.; Mozafari, M.; Gaiani, C.; Linder, M. Liposomes: A Review of Manufacturing Techniques and Targeting Strategies. *Curr. Nanosci.* **2011**, *7*, 436–452.
6. Torchilin, V. P.; Omelyanenko, V. G.; Papisov, M. I.; Bogdanov, A. A., Jr.; Trubetskoy, V. S.; Herron, J. N.; Gentry, C. A. Poly(ethylene glycol) on the Liposome Surface: On the Mechanism of Polymer-Coated Liposome Longevity. *Biochim. Biophys. Acta, Biomembr.* **1994**, *1195*, 11–20.
7. Martina, M. S.; Nicolas, V.; Wilhelm, C.; Ménager, C.; Barratt, G.; Lesieur, S. The *In Vitro* Kinetics of the Interactions between PEG-ylated Magnetic-Fluid-Loaded Liposomes and Macrophages. *Biomaterials* **2007**, *28*, 4143–4153.
8. Sawant, R. R.; Torchilin, V. P. Challenges in Development of Targeted Liposomal Therapeutics. *AAPS J.* **2012**, *14*, 303–315.
9. Peer, D.; Karp, J. M.; Hong, S.; Farokhzad, O. C.; Margalit, R.; Langer, R. Nanocarriers as an Emerging Platform for Cancer Therapy. *Nat. Nanotechnol.* **2007**, *2*, 751–760.
10. Chang, H. I.; Yeh, M. K. Clinical Development of Liposome-Based Drugs: Formulation, Characterization, and Therapeutic Efficacy. *Int. J. Nanomed.* **2012**, *7*, 49–60.
11. Ganta, S.; Devalapally, H.; Shahiwala, A.; Amiji, M. A Review of Stimuli-Responsive Nanocarriers for Drug and Gene Delivery. *J. Controlled Release* **2008**, *126*, 187–204.
12. Brown, S. B.; Brown, E. A.; Walker, I. The Present and Future Role of Photodynamic Therapy in Cancer Treatment. *Lancet Oncol.* **2004**, *5*, 497–508.
13. Tu, H. L.; Lin, Y. S.; Lin, H. Y.; Hung, Y.; Lo, L. W.; Chen, Y. F.; Mou, C. Y. *In Vitro* Studies of Functionalized Mesoporous Silica Nanoparticles for Photodynamic Therapy. *Adv. Mater.* **2009**, *21*, 172–177.
14. Taillefer, J.; Brasseur, N.; van Lier, J. E.; Lenaerts, V.; Garrec, D. L.; Leroux, J. C. *In-Vitro* and *In-Vivo* Evaluation of pH-Responsive Polymeric Micelles in a Photodynamic Cancer Therapy Model. *J. Pharm. Pharmacol.* **2001**, *53*, 155–166.
15. Fowley, C.; Nomikou, N.; McHale, A. P.; McCaughan, B.; Callan, J. F. Extending the Tissue Penetration Capability of Conventional Photosensitisers: A Carbon Quantum Dot-Protoporphyrin IX Conjugate for Use in Two-Photon Excited Photodynamic Therapy. *Chem. Commun.* **2013**, *49*, 8934–8936.
16. Choi, W. I.; Kim, J. Y.; Kang, C.; Byeon, C. C.; Kim, Y. H.; Tae, G. Tumor Regression *in Vivo* by Photothermal Therapy Based on Gold-Nanorod-Loaded, Functional Nanocarriers. *ACS Nano* **2011**, *5*, 1995–2003.
17. Cole, J. R.; Mirin, N. A.; Knight, M. W.; Goodrich, G. P.; Halas, N. J. Photothermal Efficiencies of Nanoshells and Nanorods for Clinical Therapeutic Applications. *J. Phys. Chem. C* **2009**, *113*, 12090–12094.
18. Zhang, Z.; Wang, J.; Chen, C. Near-Infrared Light-Mediated Nanoplatforms for Cancer Thermo-Chemotherapy and Optical Imaging. *Adv. Mater.* **2013**, *25*, 3869–3880.
19. Schnarr, K.; Mooney, R.; Weng, Y. M.; Zhao, D. H.; Garcia, E.; Armstrong, B.; Annala, A. J.; Kim, S. U.; Aboody, K. S.; Berlin, J. M. Gold Nanoparticle-Loaded Neural Stem Cells for Photothermal Ablation of Cancer. *Adv. Healthcare Mater.* **2013**, *2*, 976–982.
20. Shen, H. F.; You, J.; Zhang, G. D.; Ziemys, A.; Li, Q. P.; Bai, L. T.; Deng, X. Y.; Erm, D. R.; Liu, X. W.; Li, C.; et al. Cooperative, Nanoparticle-Enabled Thermal Therapy of Breast Cancer. *Adv. Healthcare Mater.* **2012**, *1*, 84–89.
21. Johannsen, M.; Gneveckow, U.; Eckelt, L.; Feussner, A.; Waldöfner, N.; Scholz, R.; Deger, S.; Wust, P.; Loening, S.; Jordan, A. Clinical Hyperthermia of Prostate Cancer Using Magnetic Nanoparticles: Presentation of a New Interstitial Technique. *Int. J. Hyperthermia* **2005**, *21*, 637–647.
22. Shi, D.; Cho, H. S.; Chen, Y.; Xu, H.; Gu, H.; Lian, J.; Wang, W.; Liu, G.; Huth, C.; Wang, L.; et al. Fluorescent Polystyrene–Fe_3O_4 Composite Nanospheres for *In Vivo* Imaging and Hyperthermia. *Adv. Mater.* **2009**, *21*, 2170–2173.
23. Brulé, S.; Levy, M.; Wilhelm, C.; Letourneur, D.; Gazeau, F.; Ménager, C.; Le Visage, C. Doxorubicin Release Triggered by Alginate Embedded Magnetic Nanoheaters: A Combined Therapy. *Adv. Mater.* **2011**, *23*, 787–790.
24. Lopez-Noriega, A.; Hastings, C. L.; Ozbakir, B.; O'Donnell, K. E.; O'Brien, F. J.; Storm, G.; Hennink, W. E.; Duffy, G. P.; Ruiz-Hernandez, E. Hyperthermia-Induced Drug Delivery from Thermosensitive Liposomes Encapsulated in an Injectable Hydrogel for Local Chemotherapy. *Adv. Healthcare Mater.* **2014**, *3*, 854–859.
25. Kolosnjaj-Tabi, J.; Di Corato, R.; Lartigue, L.; Marangon, I.; Guardia, P.; Silva, A. K. A.; Luciani, N.; Clement, O.; Flaud, P.; Singh, J. V.; et al. Heat-Generating Iron Oxide Nanocubes: Subtle "Destructurators" of the Tumoral Microenvironment. *ACS Nano* **2014**, *8*, 4268–4283.
26. Bovis, M. J.; Woodhams, J. H.; Loizidou, M.; Scheglmann, D.; Bown, S. G.; MacRobert, A. J. Improved *In Vivo* Delivery of M-Thpc *via* Pegylated Liposomes for Use in Photodynamic Therapy. *J. Controlled Release* **2012**, *157*, 196–205.
27. Amstad, E.; Kohlbrecher, J.; Müller, E.; Schweizer, T.; Textor, M.; Reimhult, E. Triggered Release from Liposomes through Magnetic Actuation of Iron Oxide Nanoparticle Containing Membranes. *Nano Lett.* **2011**, *11*, 1664–1670.
28. Soenen, S. J.; Velde, G. V.; Ketkar-Atre, A.; Himmelreich, U.; De Cuyper, M. Magnetoliposomes as Magnetic Resonance Imaging Contrast Agents. *Wiley Interdiscip. Rev.: Nanomed. Nanobiotechnol.* **2011**, *3*, 197–211.
29. Mikhaylov, G.; Mikac, U.; Magaeva, A. A.; Itin, V. I.; Naiden, E. P.; Psakhye, I.; Babes, L.; Reinheckel, T.; Peters, C.; Zeiser, R. Ferri-liposomes as an MRI-Visible Drug-Delivery System for Targeting Tumours and Their Microenvironment. *Nat. Nanotechnol.* **2011**, *6*, 594–602.
30. Béalle, G.; Di Corato, R.; Kolosnjaj-Tabi, J.; Dupuis, V.; Clément, O.; Gazeau, F.; Wilhelm, C.; Ménager, C. Ultra Magnetic Liposomes for MR Imaging, Targeting, and Hyperthermia. *Langmuir* **2012**, *28*, 11834–11842.
31. Yanase, M.; Shinkai, M.; Honda, H.; Wakabayashi, T.; Yoshida, J.; Kobayashi, T. Intracellular Hyperthermia for Cancer Using Magnetite Cationic Liposomes: An *In Vivo* Study. *Cancer Sci.* **1998**, *89*, 463–470.
32. Pradhan, P.; Giri, J.; Rieken, F.; Koch, C.; Mykhaylyk, O.; Döblinger, M.; Banerjee, R.; Bahadur, D.; Plank, C. Targeted Temperature Sensitive Magnetic Liposomes for Thermo-Chemotherapy. *J. Controlled Release* **2010**, *142*, 108–121.
33. Senge, M. O.; Brandt, J. C. Temoporfin (Foscan®, 5,10,15,20-Tetra(m-hydroxyphenyl)chlorin)—A Second-Generation Photosensitizer. *Photochem. Photobiol.* **2011**, *87*, 1240–1296.
34. Karakullukcu, B.; Nyst, H. J.; van Veen, R. L.; Hoebers, F. J.; Hamming-Vrieze, O.; Witjes, M. J.; de Visscher, S. A.; Burlage, F. R.; Levendag, P. C.; Sterenborg, H. J. mTHPC Mediated Interstitial Photodynamic Therapy of Recurrent Nonmetastatic Base of Tongue Cancers: Development of a New Method. *Head Neck* **2012**, *34*, 1597–1606.
35. Fayol, D.; Luciani, N.; Lartigue, L.; Gazeau, F.; Wilhelm, C. Managing Magnetic Nanoparticle Aggregation and Cellular Uptake: A Precondition for Efficient Stem-Cell Differentiation and MRI Tracking. *Adv. Healthcare Mater.* **2013**, *2*, 313–325.
36. Aubertin, K.; Bonneau, S.; Silva, A. K. A.; Bacri, J.-C.; Gallet, F.; Wilhelm, C. Impact of Photosensitizers Activation on Intracellular Trafficking and Viscosity. *PLoS One* **2013**, *8*, e84850.
37. Das, K.; Dube, A.; Gupta, P. A Spectroscopic Study of Photobleaching of Chlorin P6 in Different Environments. *Dyes Pigm.* **2005**, *64*, 201–205.

38. Busch, T. M.; Hahn, S. M.; Evans, S. M.; Koch, C. J. Depletion of Tumor Oxygenation during Photodynamic Therapy: Detection by the Hypoxia Marker Ef3 [2-(2-Nitroimidazol-1[H]-Yl)-*N*-(3,3,3-trifluoropropyl)acetamide]. *Cancer Res.* **2000**, *60*, 2636–2642.
39. Orenstein, A.; Kostenich, G.; Kopolovic, Y.; Babushkina, T.; Malik, Z. Enhancement of Ala-PDT Damage by IR-Induced Hyperthermia on a Colon Carcinoma Model. *Photochem. Photobiol.* **1999**, *69*, 703–707.
40. Yanase, S.; Nomura, J.; Matsumura, Y.; Nagata, T.; Fujii, T.; Tagawa, T. Synergistic Interaction of 5-Aminolevulinic Acid-Based Photodynamic Therapy with Simultaneous Hyperthermia in an Osteosarcoma Tumor Model. *Int. J. Oncol.* **2006**, *29*, 365–373.
41. Frank, J.; Lambert, C.; Biesalski, H. K.; Thews, O.; Vaupel, P.; Kelleher, D. K. Intensified Oxidative and Nitrosative Stress Following Combined Ala-Based Photodynamic Therapy and Local Hyperthermia in Rat Tumors. *Int. J. Cancer* **2003**, *107*, 941–948.
42. Lin, J.; Wang, S.; Huang, P.; Wang, Z.; Chen, S.; Niu, G.; Li, W.; He, J.; Cui, D.; Lu, G. Photosensitizer-Loaded Gold Vesicles with Strong Plasmonic Coupling Effect for Imaging-Guided Photothermal/Photodynamic Therapy. *ACS Nano* **2013**, *7*, 5320–5329.
43. Jang, B.; Park, J.-Y.; Tung, C.-H.; Kim, I.-H.; Choi, Y. Gold Nanorod−Photosensitizer Complex for Near-Infrared Fluorescence Imaging and Photodynamic/Photothermal Therapy *in Vivo*. *ACS Nano* **2011**, *5*, 1086–1094.
44. Wang, J.; Zhu, G.; You, M.; Song, E.; Shukoor, M. I.; Zhang, K.; Altman, M. B.; Chen, Y.; Zhu, Z.; Huang, C. Z. Assembly of Aptamer Switch Probes and Photosensitizer on Gold Nanorods for Targeted Photothermal and Photodynamic Cancer Therapy. *ACS Nano* **2012**, *6*, 5070–5077.
45. Wang, S.; Huang, P.; Nie, L.; Xing, R.; Liu, D.; Wang, Z.; Lin, J.; Chen, S.; Niu, G.; Lu, G.; et al. Single Continuous Wave Laser Induced Photodynamic/Plasmonic Photothermal Therapy Using Photosensitizer-Functionalized Gold Nanostars. *Adv. Mater.* **2013**, *25*, 3055–3061.
46. Oliveira, D. M.; Macaroff, P. P.; Ribeiro, K. F.; Lacava, Z. G. M.; Azevedo, R. B.; Lima, E. C. D.; Morais, P. C.; Tedesco, A. C. Studies of Zinc Phthalocyanine/Magnetic Fluid Complex as a Bifunctional Agent for Cancer Treatment. *J. Magn. Magn. Mater.* **2005**, *289*, 476–479.
47. Corr, S. A.; O'Byrne, A.; Gun'ko, Y. K.; Ghosh, S.; Brougham, D. F.; Mitchell, S.; Volkov, Y.; Prina-Mello, A. Magnetic-Fluorescent Nanocomposites for Biomedical Multitasking. *Chem. Commun.* **2006**, *43*, 4474–4476.
48. de Paula, L. B.; Primo, F. L.; Jardim, D. R.; Morais, P. C.; Tedesco, A. C. Development, Characterization, and *In Vitro* Trials of Chloroaluminum Phthalocyanine-Magnetic Nanoemulsion to Hyperthermia and Photodynamic Therapies on Glioblastoma as a Biological Model. *J. Appl. Phys.* **2012**, *111*, 07B307.
49. Bolfarini, G. C.; Siqueira-Moura, M. P.; Demets, G. J. F.; Morais, P. C.; Tedesco, A. C. *In Vitro* Evaluation of Combined Hyperthermia and Photodynamic Effects Using Magneto-liposomes Loaded with Cucurbit 7 Uril Zinc Phthalocyanine Complex on Melanoma. *J. Photochem. Photobiol., B* **2012**, *115*, 1–4.
50. Massart, R. Preparation of Aqueous Magnetic Liquids in Alkaline and Acidic Media. *IEEE Trans. Magn.* **1981**, *17*, 1247–1248.
51. Szoka, F.; Papahadjopoulos, D. Procedure for Preparation of Liposomes with Large Internal Aqueous Space and High Capture by Reverse-Phase Evaporation. *Proc. Natl. Acad. Sci. U.S.A.* **1978**, *75*, 4194–4198.
52. Rouser, G.; Fleischer, S.; Yamamoto, A. Two Dimensional Thin Layer Chromatographic Separation of Polar Lipids and Determination of Phospholipids by Phosphorus Analysis of Spots. *Lipids* **1970**, *5*, 494–496.